Electronic Supplementary Material (ESI) for Lab on a Chip.
This journal is © The Royal Society of Chemistry 2017

Supplementary Information

Automatic concentration and reformulation of PET tracers via microfluidic membrane distillation

Philip H. Chao[1,2], Jeffery Collins[2,3], Joseph P. Argus [3,] , Wei-Yu Tseng[2,3], Jason T. Lee[2,3], R. Michael van Dam[1,2,3]

[1]Department of Bioengineering, Henry Samueli School of Engineering, UCLA, Los Angeles, CA, USA
[2]Crump Institute for Molecular Imaging, David Geffen School of Medicine, UCLA, Los Angeles, CA, USA
[3] Department of Molecular & Medical Pharmacology, David Geffen School of Medicine, UCLA, Los Angeles, CA,

Table of Contents

1 Characterization of final collected volume after evaporation delay 2
2 Contact angle measurements 2
3 Measuring breakthrough pressure (BTP) 2
4 Assessing stability of radiolabeled molecules 5
5 GC-MS determination of solvent content 6
6 Theoretical vapor pressures that may affect BTP measurements 7
7 Optimization of operating conditions 8
8 Evaporation rate of rotary evaporator 9
9 Additional designs considered for optimization of heating 11
9.1 Overview of designs 11
9.2 Comparison of evaporation rates 11
9.3 Comparison of surface temperatures 13
10 Characterization of dynamic evaporation rates for large sample volumes 14
11 Surface roughness characterization 15
12 Total operating time 15
13 In vivo mouse imaging of [^{18}F]D-FAC 16
14 References 17

1 Characterization of final collected volume after evaporation delay

The final volume of collected sample (or rinse solution) can be adjusted by continuing to evaporate, even after the sample has shrunk to the point where it fits entirely within the chip. We measured the recovered volume to determine the additional evaporation delay needed to reduce the volume <0.5 mL. The chip was preheated to 100°C, and other parameters were set to values described in the main text. For each measurement, 4 mL of water was loaded into the sample reservoir. The extra delay time was set in the automated concentration program, and the number of rinses was set to zero. After completion of the automated concentration process, the volume of the collected product was measured using a 1mL pipette (P1000 Pipetman, Gilson Inc., Middleton, WI, USA). Samples with volumes larger than 1mL were measured by first removing and counting 1.0 mL portions. The remaining volume was measured by aspirating into the pipette and adjusting the volume setting until it matched the sample volume (i.e. with no additional air aspirated into the tip). 50 sec was sufficient to achieve a collected volume <0.5 mL.

2 Contact angle measurements

Contact angle of droplets of various solvent compositions were measured at different temperatures. For each condition, a 1 cm x 1 cm square piece of 0.2 µm PTFE membrane (Sterlitech, Kent, WA, USA) was placed on top of a heated aluminum block with an embedded cartridge heater (8376T27, McMaster Carr, Santa Fe Springs, CA, USA) and K-type thermocouple (5TC-GG-(K)-30-(72), OMEGA Engineering, Inc., Stamford, CT, USA). Temperature was controlled via a PID controller (CN7500, OMEGA Engineering, Inc, Stamford, CT, USA). After preheating the membrane for 1 min, a 5 µL sample was pipetted onto the membrane surface and a side-view image was taken with a digital camera (Canon Rebel XT, Canon, Irvine, CA USA) with a Canon MP-E 65mm 1-5x macro lens. Contact angle was determined from each photograph with ImageJ software (U.S. National Institute of Health, Bethesda, MD, USA) using a plugin called Low-Bond Axisymmetric Drop Shape Analysis (LBADSA). Three replicates (load new membrane, preheat, pipette droplet, image and analyze) were performed for each sample condition and averaged to produce a representative value. Results are shown in

Figure S1.

Figure S1: Contact angle measurements for (A) EtOH and (B) MeCN mixtures with water at different temperatures. Each data point represents the average of n=3 replicates; error bars represent the standard deviation. The red line represents a contact angle of 90°, the barrier between wetting and nonwetting.

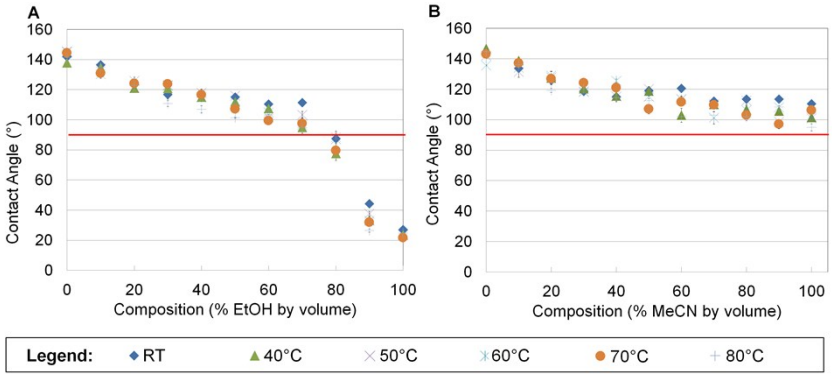

3 Measuring breakthrough pressure (BTP)

To directly measure BTP, a custom temperature-controlled test fixture (described below) was built to hold small pieces of the membrane material. One side of each membrane was exposed to the desired

sample at a controlled pressure; the other side was vented to atmospheric pressure. On the input side, a tubing connection is made from a sample reservoir (Falcon 15 mL conical tube, BD Biosciences, San Jose, CA, USA) to the testing fixture. The sample was manually primed up to the membrane via syringe and then the sample pressure was controlled with a pressure regulator (ITV0010, SMC Corporation, Japan) and monitored with a pressure gauge (MLH-050PGB01E, Honeywell International Inc. Golden Valley, MN, USA). These two components were connected to a laptop via a data acquisition module (NI USB-6212, National Instruments, Austin, TX, USA) and were controlled using a custom LabVIEW program. A fluidic flow sensor (SLI-2000, Sensirion Westlake Village, CA, USA) was positioned along the input tubing.

Flow rate was monitored as pressure was increased automatically from 0.0 to 13.5 psi in 0.3 psi increments. (The maximum tested pressure was 13.5 psi, because when higher pressures are used in the chip, severe membrane deformation that causes blocking of the gas flow layer is observed.) After each change in pressure, there was an 8s delay to allow for equilibration, and then the pressure and flow rate were recorded. In general, fluid flow rate stayed close to ~0.0 mL/min below breakthrough, but increased dramatically upon reaching the breakthrough pressure, ultimately reaching the maximum reading limit of the sensor (5 mL/min).

BTP was identified as the point on a plot of flow rate versus pressure where the flow measurement exceeded a threshold value, 25μL/min, corresponding to the worst-case measurement error specified for the sensor. The pressure corresponding to the threshold flow rate was interpolated by performing a fit of flow rate versus pressure between the closest points on either side of the threshold. The BTP identification process can be seen in **Figure S2**.

Figure S2: Determination of BTP. Fluid flow rate is plotted as a function of pressure. BTP is defined as the point where the flow rate exceeds the threshold value (25μL/min; red line). BTP was interpolated from adjacent data points after first performing a linear fit (blue dotted line).

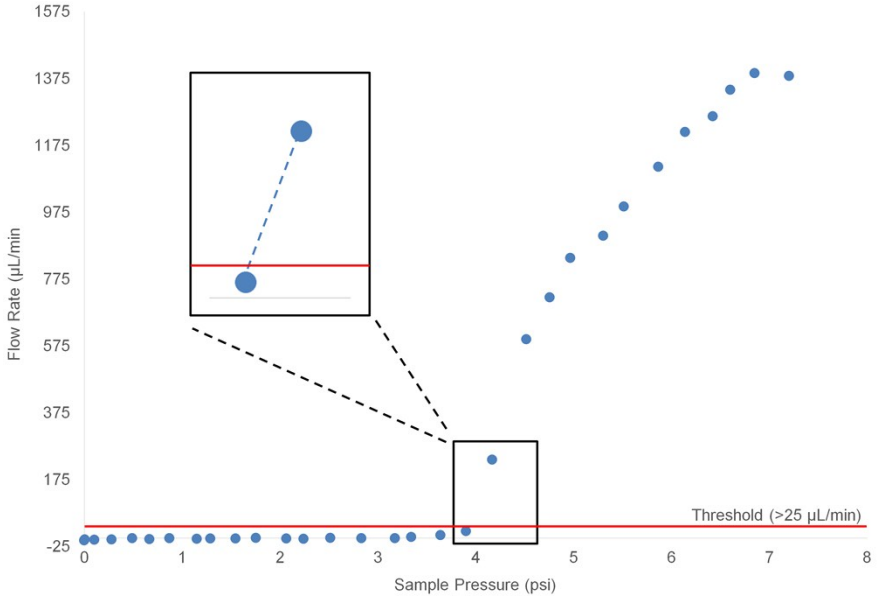

The testing fixture was built out of 6061 aluminum alloy and could split apart into two halves. One half contained four individual wells. Membrane samples (cut slightly larger than the wells) were inserted into each well, followed by a square profile rubber o-ring (4061T115, McMaster-Carr, Santa Fe Springs, CA,

USA). The second half of the fixture was then secured via nine bolts to secure the membranes in place. The fixture and experimental setup are shown in **Figure S3**.

Initially, heating was performed by placing the fixture inside a convective oven (Isotemp Oven Model# 825F, Fisher Scientific, Pittsburgh, PA, USA). Heat transfer from the air within the oven to the chip, however, was not sufficient to maintain the internal temperature of the aluminum fixture during operation. Thus, two heater blocks were mounted on the top and bottom of the fixture, each containing one 100W cartridge heater (8376T27, McMaster Carr) as well as one K-type thermocouple (5TC-GG-(K)-30-(72), OMEGA Engineering, Inc., Stamford, CT). Heaters and thermocouples were coated with thermal paste (OT-201-2, OMEGA Engineering, Inc., Stamford, CT) before insertion into the block. Temperature of each heater block was independently maintained via a PID temperature controller (CN7500, OMEGA Engineering, Inc., Stamford, CT). The combination of heating blocks and oven heating resulted in stable temperatures.

Figure S3: (A) Schematic of custom-built fixture for testing the breakthrough pressure of membrane samples at different temperatures. (B) Experimental setup for measuring breakthrough pressure with the test fixture.

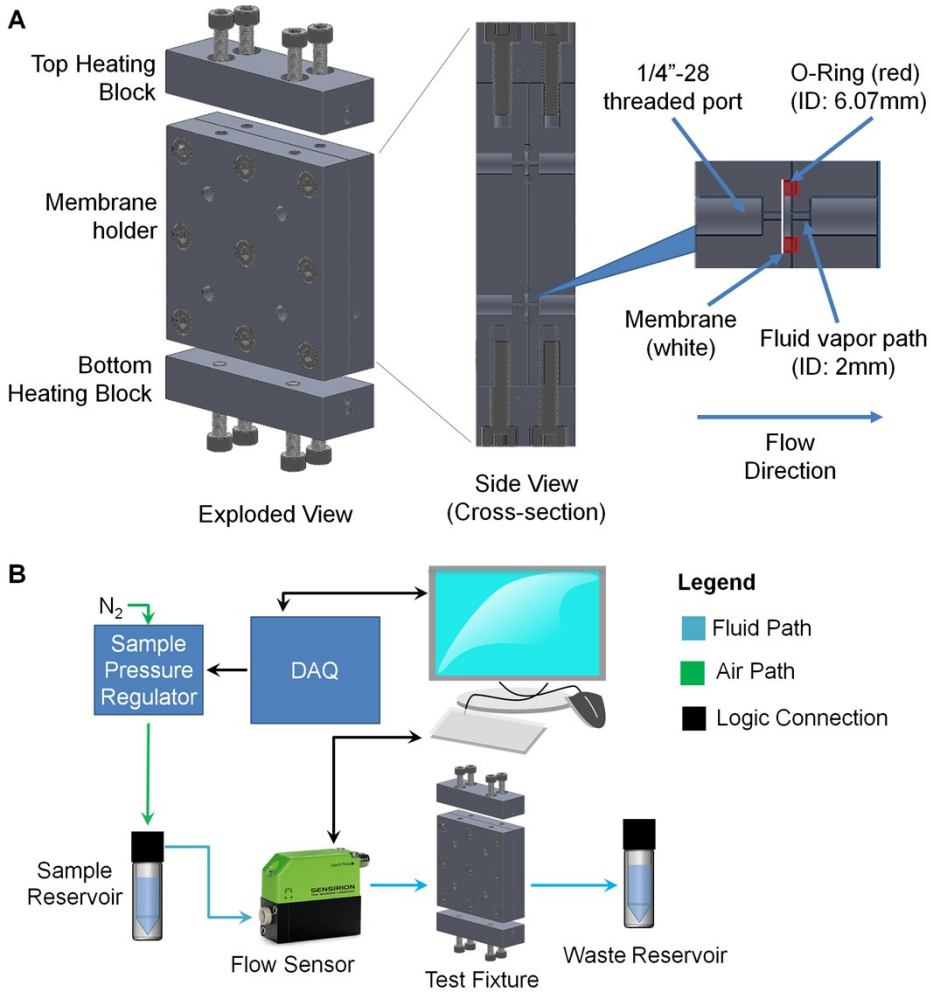

4 Assessing stability of radiolabeled molecules

Radiochemical stability of tracers under microfluidic concentration conditions was determined via analytical radio-HPLC comparison of samples before and after concentration. Analytical HPLC was performed on a Smartline HPLC system (Knauer, Berlin, Germany) with an inline ultraviolet (254 nm) detector (Knauer, Berlin, Germany) and a gamma-radiation coincidence detector and counter (B-FC-4100 and BFC-1000; Bioscan, Inc., Poway, CA, USA). Separations were performed using a Luna C18 column (5 µm particle size, 4.6 x 250 mm; 00G-4252-E0, Phenomenex, Torrance, CA, USA) according to the conditions in **Table S1**. Chromatograms were collected by a GinaStar analog-to-digital converter (Raytest Inc., Straubenhardt, Germany) and GinaStar software. The purified product peak was verified by co-injection of non-radioactive standard, and purity was quantified by calculating the area in the product peak divided by the area of all peaks in the chromatogram.

Table S1: Analytical HPLC conditions for PET tracers and prosthetic groups.

Tracer	Analytical HPLC mobile phase composition (all ratios are v:v)	Flow Rate (mL/min)	Purification Method
[^{18}F]D-FAC	10:90 EtOH / 50 mM NH_4OAc	1.0	Isocratic
[^{18}F]FHBG	10:90 MeCN / 50mM NH_4OAc	1.0	Isocratic
[^{18}F]D-FEAU	15:85 MeCN / water	1.0	Isocratic
[^{18}F]FBEM	5:95 MeCN / water at 0 min 35:65 MeCN / water at 35 min	1.0	Gradient
[^{18}F]Fallypride	60:40 MeCN / 25mM NH_4HCO_2 with 1%TEA	1.0	Isocratic

Chromatograms for the various tracers are shown in **Figure S4**. No differences in radiochemical purity were observed for [^{18}F]FHBG, [^{18}F]D-FAC, and [^{18}F]FBEM, indicating stability at 100°C. These were all concentrated via the partial evaporation method. Note the [^{18}F]FBEM chromatogram shows a small impurity corresponding to hydrolyzed [^{18}F]FBEM. This may suggest a very slight amount of degradation during the concentration process. [^{18}F]D-FEAU and [^{18}F]Fallypride were concentrated via the complete evaporation method and recovered in saline. No differences in chromatograms were observed before and after concentration, indicating these molecules are stable under the concentration conditions. The chromatogram for [^{18}F]D-FEAU showed a slight shift in retention times for samples before and after concentration, but followup co-injection studies confirmed that the peak corresponds to the same molecule.

Figure S4: Radio-chromatograms to assess radiochemical purity of PET tracers before and after microfluidic concentration. (A) [^{18}F]D-FAC. (B) [^{18}F]FHBG. (C) [^{18}F]FBEM. (D) [^{18}F]Fallypride. (E) [^{18}F]D-FEAU.

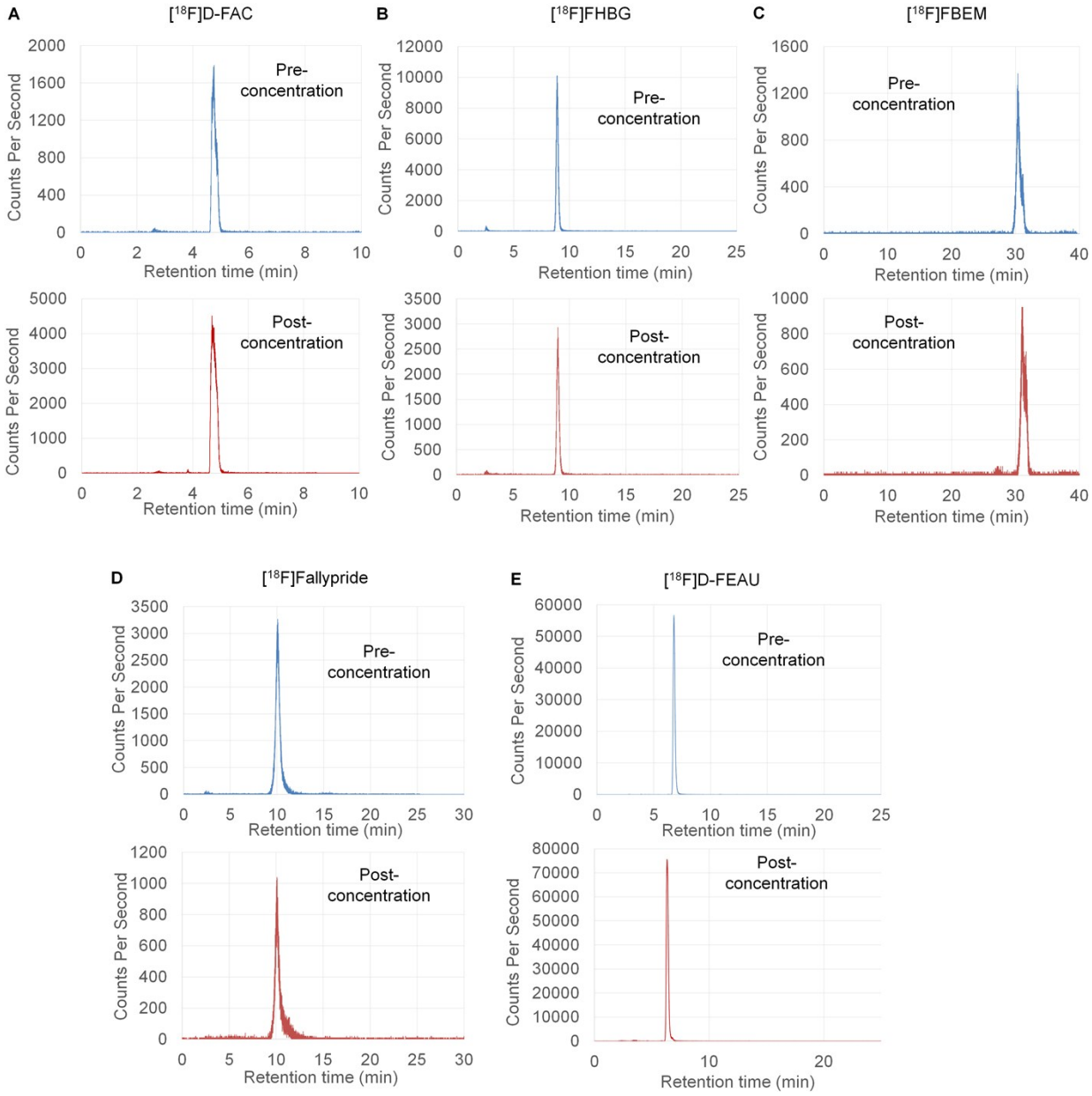

5 GC-MS determination of solvent content

Samples and standards were analyzed using an Agilent 7890A GC system equipped with an Agilent DB-Wax column (122-7033) connected to an Agilent 5975C MSD run in electron ionization (EI) mode at 70 eV. 0.5 µL of the sample (or standard) was injected at a 1:200 split ratio. The carrier gas was helium and the column flow rate was maintained at 1 mL/min. The transfer line, MS source, and quadrupole temperatures were 250°C, 230°C, and 150°C, respectively, and the detector was run in SIM mode. For acetonitrile (MeCN) and ethanol (EtOH) the inlet temperature was set to 250°C. The GC oven temperature started at 70°C for 6.5 min, then was increased to 240°C at 85°C/min and held for 1.5 min. Analysis of DMSO was done at a later time and was performed with a modified method. Samples

containing DMSO were injected in 0.5 µL volume at a 1:200 split ratio. The inlet temperature used for injection of DMSO was 200°C. For the analysis of DMSO, the GC oven temperature started at 50°C for 1 min, then was increased to 220°C at 25°C/min and held for 5 min. MeCN, EtOH, and DMSO were monitored at 41,31 and 63 m/z peaks, respectively. Area under the curve (AUC) quantitation was conducted on ChemStation software (Agilent). Residual solvent concentration was calculated by fitting sample AUCs to the appropriate standard curve.

Piecewise standard curves of AUC versus sample composition were produced for each type of solvent. The standards of EtOH and MeCN with solvent composition ranging from 0.0-0.3% (v/v) show high linearity resulting in the use of a linear fit for AUCs that fall within this region. A second piece of the standard curve was generated for interpolating compositions above 0.3% (up to 10%) and was based on a higher order parabolic fit. The parabolic fit, however, still includes the low end composition values (0 – 0.3%). AUCs that fall above the 0.3% AUC value are fitted with this second piece of the standard curve. For DMSO, high linearity was seen in solvent compositions ranging from 0.0-1.0% (v/v), and a higher order fit was used for interpolating compositions above 1% (up to 10%).

Figure S5: Standard curve comparing AUC and organic solvent composition for (A) MeCN, (B) EtOH and (C) DMSO. The dotted line represents the transition between linear fit for low solvent concentrations and the higher order fit used for higher solvent concentrations.

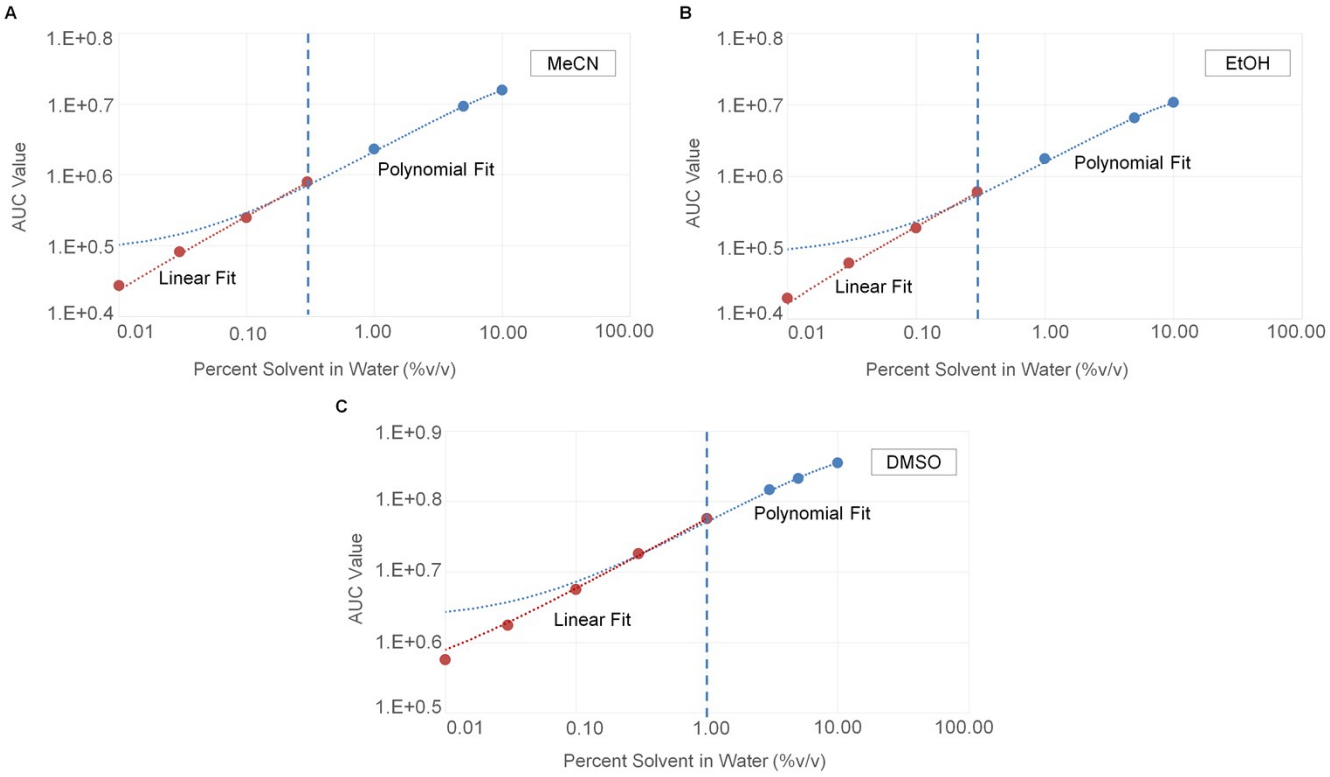

6 Theoretical vapor pressures that may affect BTP measurements

Theoretical vapor pressures of solvent mixtures (**Table S2**) were calculated using Raoult's Law. Raoult's Law states that the vapor pressure of a mixture is the sum of the partial vapor pressures of the solute (e.g. MeCN and EtOH) and solvent (e.g. water) [1]. Each partial vapor pressure is the vapor pressure of the pure compound [2] multiplied by the mole fraction in the mixture.

Table S2: Vapor pressure as a function of temperature for various mobile phase compositions based on (A) MeCN and (B) EtOH. Reported values are in psi.

A

% MeCN in H_2O (v/v)	Temperature (°C)				
	RT	40	60	80	100
0	0.46	1.07	2.89	6.88	14.71
10	0.53	1.24	3.15	7.15	15.06
20	0.60	1.42	3.45	7.46	15.46
30	0.69	1.64	3.79	7.83	15.93
40	0.79	1.90	4.20	8.25	16.48
50	0.92	2.21	4.68	8.77	17.14
60	1.07	2.58	5.27	9.39	17.94
70	1.25	3.05	6.01	10.16	18.93
80	1.49	3.64	6.94	11.15	20.20
90	1.80	4.43	8.17	12.45	21.87
100	2.24	5.51	9.88	14.24	24.18

B

% EtOH in H_2O (v/v)	Temperature (°C)				
	RT	40	60	80	100
0	0.46	1.07	2.89	6.88	14.71
10	0.48	1.12	3.02	7.17	15.30
20	0.51	1.18	3.18	7.51	15.99
30	0.54	1.25	3.35	7.91	16.81
40	0.58	1.33	3.57	8.39	17.77
50	0.62	1.44	3.82	8.97	18.94
60	0.68	1.56	4.14	9.68	20.39
70	0.75	1.72	4.54	10.59	22.23
80	0.84	1.92	5.07	11.78	24.63
90	0.97	2.21	5.79	13.40	27.92
100	1.15	2.62	6.84	15.75	32.68

7 Optimization of operating conditions

The effect of gas-flow pressure differential ($P_{gas_out} - P_{gas_in}$) and sample pressure (P_{sample}) on the evaporation rate was explored (**Figure S6**) in order to optimize performance.

Increased gas-flow pressure differential will proportionately increase the volumetric flow rate of gas in the gas-flow channel. It is expected that increased gas flow helps to remove vapor and thus reduce the partial pressure of solvent vapor on the gas-flow side of the membrane, and thereby promote increased evaporation and movement of vapor across the membrane. Indeed, this was observed experimentally suggesting that the maximum allowable gas flow (that satisfies operating constraints) should be used.

In contrast, the sample pressure was found to have negligible effect on evaporation rate. This indicates that even the lowest sample pressure is sufficient to ensure that the sample channel within the chip remains full of sample during the concentration process.

Figure S6: (A) Evaporation rates as a function of gas flow differential in the gas flow layer with the system operated at different temperature set points. (B) Evaporation rates as a function of sample inlet pressure (performed at 100°C).

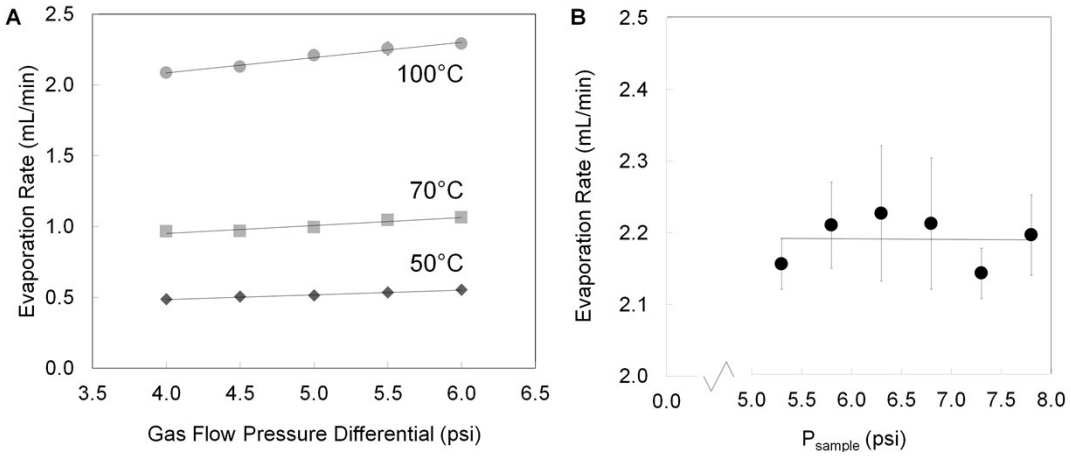

8 Evaporation rate of rotary evaporator

A schematic of the experimental setup is shown in **Figure S7**. A vacuum pump (2010 SD Pascal, Adixen Vacuum Products, Annecy Cedex, France), is connected via a vacuum trap (CG-4516-01, Chemglass Inc., Vineland, NJ) to a remote-controlled rotary evaporator customized for radiochemistry use. Inline between the pump and the trap are a manual vacuum regulator (VR1000-N01, Poweraire, Anaheim, CA) and digital pressure gauge (ISE30A-N01-C, SMC Corporation). Water bath temperatures were selected to match temperatures tested in the microfluidic concentrator. Operation at 100°C was omitted as maintaining the rotary evaporator water bath at this temperature was not possible. Vacuum pressures during operation were chosen based on the 20/40/60 rule set by Buchi Inc. [3], [4] The 20/40/60 rule states that enough vacuum should be applied to the sample such that the effective boiling point of the sample is 20°C lower than that of the set point temperature. Vacuum pressures used for this experiment based off of the vapor pressure of water (used as the sample) can be seen in **Table S3**. In the case of 40-60°C set point temperatures our vacuum pump was unable to reach the desired vacuum levels; instead, the vacuum pump was set to the maximum vacuum level (-920 mBar) for each temperature, corresponding to an effective boiling point of 34°C.

Figure S7: (A) Schematic of setup to measure speed of rotary evaporation. Black arrows show pneumatic and vapor path. (B) Evaporation rate of water as a function of temperature in the rotary evaporator and the microfluidic concentrator with PEEK sample layer. (C) Pressure difference between vapor pressure and vacuum pressure in the rotary evaporator system during operation at each temperature.

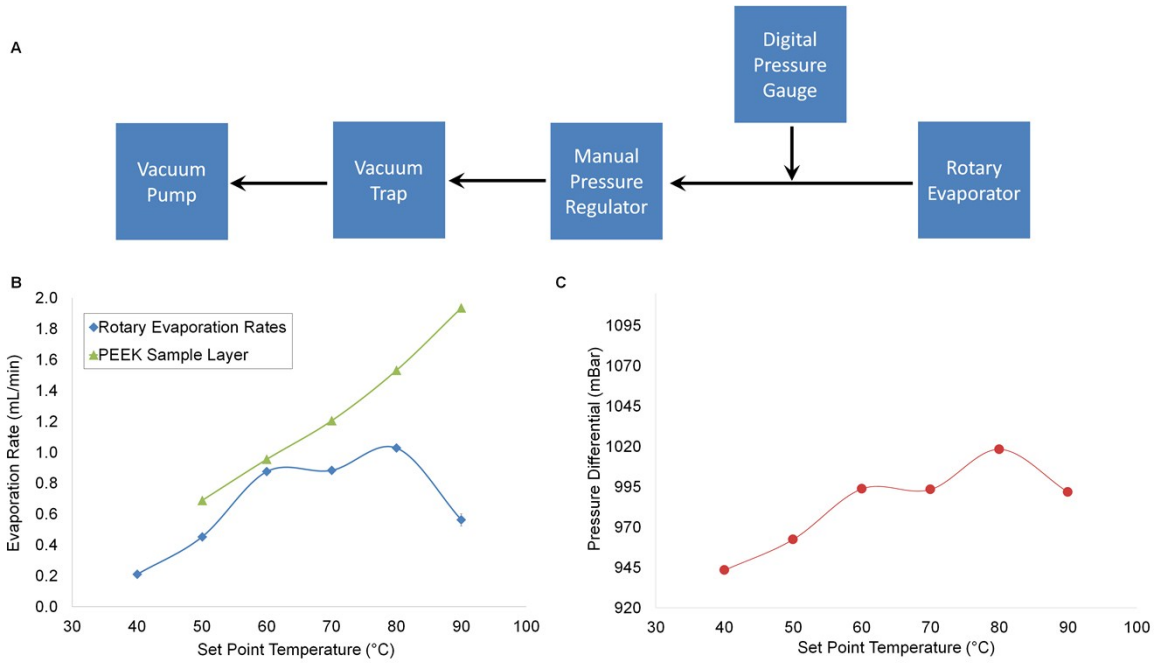

Table S3: Desired and actual operating parameters for the rotary evaporator.

Water bath setpoint (°C)	Vapor pressure of sample (mBar)	Desired effective bp of sample (°C)	Desired gauge pressure (mBar)	Applied gauge pressure (mBar)	Actual effective bp of sample (°C)
40	23.4	20	-990	-920	34
50	42.5	30	-950	-920	34
60	73.8	40	-941	-920	34
70	123	50	-870	-870	50
80	199	60	-819	-819	60
90	312	70	-680	-680	70

The results (**Figure S7**) show that the evaporation rate of the microfluidic system exceeds that of the rotary evaporator at all operating temperatures. The rotary evaporator reached a maximum evaporation rate of 1.03 ± 0.04 mL/min at 80°C. The microfluidic concentrator (with PEEK sample layer) achieved 1.53 ± 0.02 mL/min at the same temperature.

A complex relationship was observed between evaporation rate and temperature for the rotary evaporator. This behavior appears closely correlated to the resulting pressure difference between the sample vapor pressure and the vacuum pressure, suggesting that the effective driving pressure of vapor out of the rotary evaporator is the dominant factor affecting performance. It may be possible to further optimize the rotary evaporator performance by tuning operating parameters or changing the hardware configuration but this was not pursued.

9 Additional designs considered for optimization of heating

9.1 Overview of designs

Several additional chip architectures were explored that have different heat flow characteristics (**Figure S8A**). Though not characterized in detail, evaporation rates were measured for each.

1. Gas-flow layer heating. This architecture is the focus of the paper (**Figure 1**), with a 2.54 cm thick transparent acrylic support layer, 2 mm thick plastic sample layer, and a 1 cm thick 6061 aluminum alloy gas flow layer. Heating is supplied from the gas flow layer.

2. Sample layer heating. In this design, heat is applied on the sample side of the membrane by a 0.735 cm thick heating block (6061 aluminum allow) containing four 100W cartridge heaters and K-type thermocouples. The heating block was placed in direct thermal contact with the sample layer (thickness: 2 mm; channel depth: 50 μm). The gas flow layer was a 2.4 cm thick piece of Ultem, a plastic with good temperature stability, solvent resistance, and transparency.

3. Metal chip

    3.1. Metal chip with sample layer heating. This design was the same as that described in #2, except with a 1.0 cm thick 6061 aluminum alloy gas-flow layer. Heating was supplied via the metal block on the sample side of the membrane.

    3.2. Metal chip with gas-flow layer heating. This design used the same chip architecture as #3.1, except that heating was supplied via the metal gas-flow layer instead of the layer adjacent the sample layer.

    3.3. Metal chip with dual heating. This design used the same chip architecture as #3.1 and #3.2, except that heating was supplied both from the sample-side metal block as well as the metal gas-flow layer. Four 100W heaters were used, two positioned in each of the heated layers.

4. All-metal chip. This architecture was the same as #3.3, but the 2 mm thick plastic sample layer was replaced with a 3.2 mm thick 6061 aluminum alloy block. The block did not contain any channel patterns: the sample channel in this case is formed due to deflection of the permeable membrane into the channels of the gas flow layer, making room for the sample fluid.

9.2 Comparison of evaporation rates

PEEK sample layer material was chosen as the main testing material for comparing alternative heating configurations. Evaporation rates of deionized water at 100°C using the various designs are shown in **Figure S8C**.The evaporation rate of architecture #1 reported in the main paper was 2.02 ± 0.04 mL/min (n=5).

In architecture #2, with sample layer heating instead of gas-flow layer heating, the evaporation rate was significantly lower, i.e. 1.03 ± 0.01mL/min (n=5). In gas flow heating, heat must travel from the metal gas-flow layer through only the ~50 μm thick PTFE membrane to reach the contents of the sample channel. In contrast, with sample layer heating, heat must travel through the whole thickness of the sample layer minus the channel depth (i.e. 2000-50 ≈ 2000 μm of PEEK) to reach the sample. Despite the superior thermal contact area of sample layer heating (i.e. whole surface of heater is in contact with whole surface of sample layer) compared to the small contact area of gas flow heating (i.e., only at the walls between channels in the gas-flow layer), the performance of the latter is still superior, suggesting that the detrimental effect of the thick plastic layer in the heat transfer path is dominant. It is also possible that large deflection of the membrane allows it to contact the walls of the gas-flow layer during

operation, providing additional thermal contact area for gas-flow layer heating. Presumably, performance of sample layer heating could be improved if the thickness of the sample layer could be significantly reduced.

In the metal chip configuration, the plastic gas-flow layer is replaced with a metal one. With heating from the sample side (architecture #3.1), the evaporation rate was 1.38± 0.06 mL/min (n=5). Using the same layers but heating from the gas-flow side instead of sample side (architecture #3.2) increased the evaporation rate to 1.99 ± 0.03 mL/min (n=5). Overall, providing heat to the sample via the membrane (from gas-flow layer heater) is more effective than heating through the sample layer to reach the sample. By providing heating from both sides, evaporation rate was 2.22 ± 0.06 mL/min (n=5), only slightly higher than if only the gas-flow layer was heated, despite the significant extra complexity of fabrication and operation of heating from both sides.

In architecture #4, the plastic sample layer of the metal chip was replaced with a 3.2 mm thick 6061 aluminum alloy block. In this case, significant further increase in evaporation rate was observed, i.e. 3.38 ± 0.16 mL/min (n=5). The high thermal conductivity of the 6061 aluminum alloy sample layer (167 W/mK) is likely important here, consistent with the observed trend that evaporation rate in architecture #1 seems to correlate with thermal conductivity of the sample layer material (**Figure 4** of the main paper).

Figure S8: (A) Chip layer configuration for different designs (to scale), with red arrows representing the direction that heat is applied. (B) Cross-section schematics of each design, with blue arrows showing the direction of vapor transport. (C) Evaporation rates of deionized water for different designs with temperature set point at 100°C. Each bar represents the average of n=5 replicates. Error bars represent standard error of the mean.

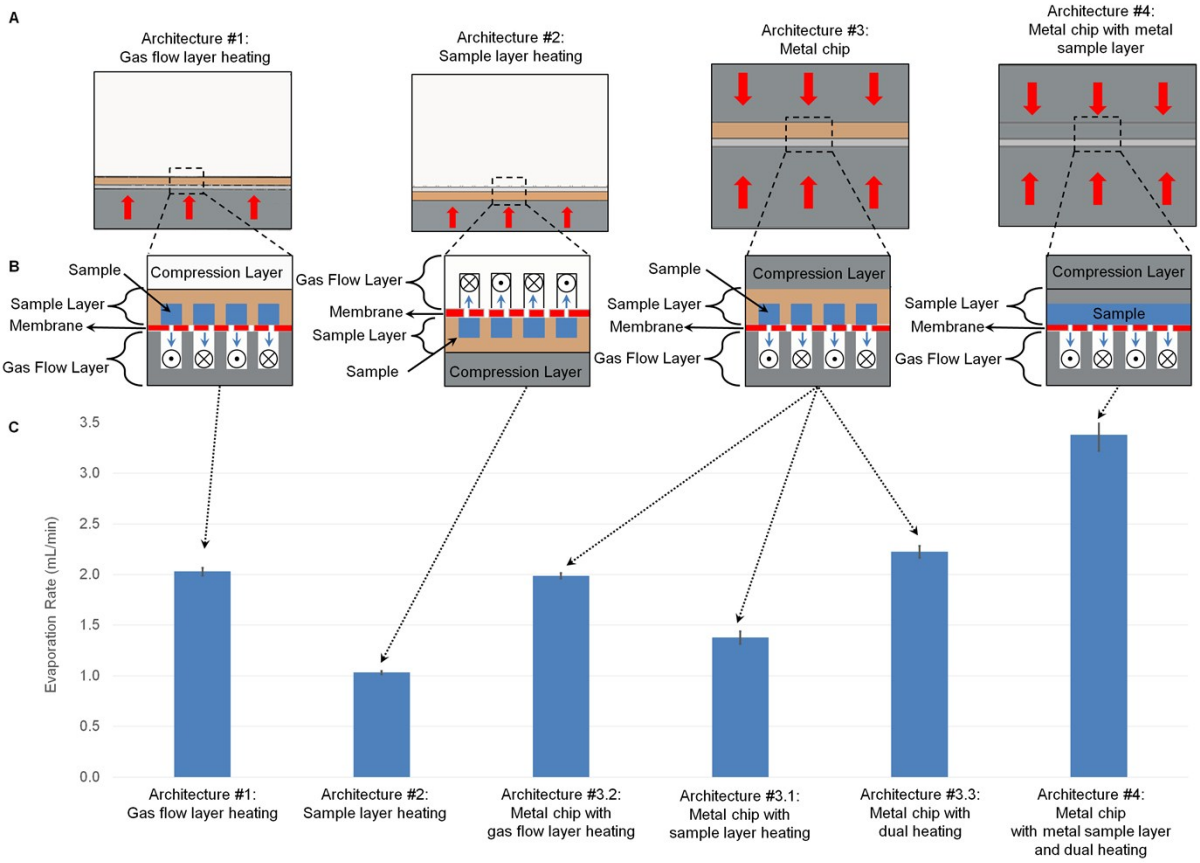

9.3 Comparison of surface temperatures

To help understand the differences in performance, we used infrared (IR) thermal imaging to measure steady-state temperatures close to the location of the sample fluid for different chip architectures. Imaging was performed with a T420 IR camera (FLIR, Boston, MA, USA). Transparent materials and reflective surfaces were coated with flat black spray paint (#51602 Krylon Industrial, Cleveland, OH, USA) in order to increase the thermal emissivity (~0.95) for imaging.

For gas flow layer heating, the gas flow layer surface that is in direct contact with the membrane was imaged. From this surface, only the thin membrane must be traversed before heat reaches the sample fluid. For sample layer heating, the membrane-contacting surface of the sample layer (i.e. where the sample channel is located) was imaged. After activating the temperature control, time was given for the temperature at the surface of interest to equilibrate. (The time to reach equilibrium was not thoroughly characterized as it is possible to pre-heat the microfluidic concentrator.) Surface temperatures were quantified by using the averaging capabilities built into the FLIR camera software. A square ROI was drawn around the channel portion of the surface being imaged, and the average temperature within this ROI was recorded (**Figure S9**). Temperature uniformity was assessed qualitatively through the generated “heat maps” as well as looking at maximum and minimum values within the ROI.

For imaging of the gas-flow layer, deviations between the measured surface temperature and the setpoint were: +0.4 °C for T_{set}=50°C, -0.1°C for T_{set}=60°C , -0.9 °C for T_{set}=70°C, -1.5°C for T_{set}=80°C , -1.7°C for T_{set}=90°C, and -2.1°C for T_{set}=100°C. On the other hand, imaging of the sample layer resulted in much larger deviations of -1.3 °C for T_{set}=50°C, -2.8°C for T_{set}=60°C , -4.8 °C for T_{set}=70°C, -6.2°C for T_{set}=80°C , -8.2 °C for T_{set}=90°C, and -9.6°C for T_{set}=100°C. Although these are surface measurements and may not reflect the actual temperatures inside an assembled device, the data suggest that when heating a plastic sample layer, the temperature of the sample fluid may be substantially lower than what can be achieved by heating through the gas-flow layer. Due to the strong dependence of evaporation rate on temperature, this temperature difference could explain why the geometries exhibit such a large difference in evaporation performance.

Figure S9: Sample IR thermal images of a (A) gas flow layer, and a (B) sample layer. Temperature measurements at individual points as well as the ROI are shown. It can be seen that for the same 100°C setpoint, temperatures in the sample layer heating architecture are significantly lower on average than temperatures in the gas flow layer heating architecture.

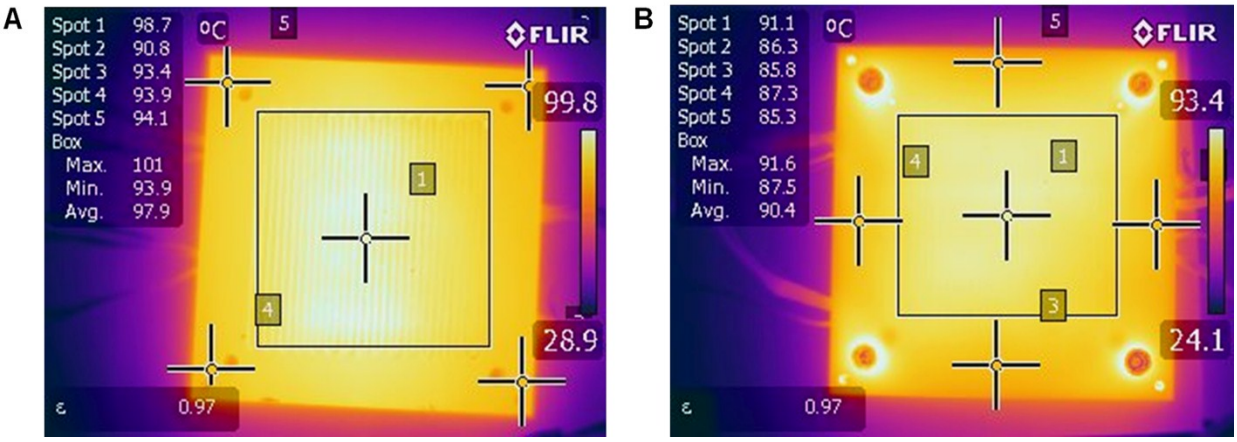

10 Characterization of dynamic evaporation rates for large sample volumes

Investigations of dynamic evaporation rate during concentration of 50 mL samples at 100°C were performed to determine if buildup of solutes or depletion of volatile organic solvent components would lead to changes in evaporation rates over time.

First, evaporation of 50 mL of deionized water was monitored as a negative control (Figure S10Figure **S10A**). Despite some fluctuations that likely represent experimental error, evaporation rate appears constant during the whole process. Indeed, no significant difference was found in statistical comparison of the average evaporation rate of the first 5 mL and the last 5 mL.

Next, concentration of NH_4OAc solutions up to 750 mM in water was performed (**Figure S10B**). Only at very high concentrations, i.e. ≥ 500mM, was a significant decrease in evaporation rate observed during the concentration process. These concentrations are ~10x higher than normally used in HPLC purification of PET tracers.

The effect of solvents were explored by concentrating samples of EtOH in water (up to 20% v/v) and MeCN in water (up to 40% v/v) (**Figure S10C,D**). Evaporation rates were found to be consistent throughout the concentration process.

Finally, as a relevant example containing both high solute content and organic solvents, we used the mobile phase for [^{18}F]FHBG (5% v/v MeCN in 50 mM NH_4OAc) (**Figure S10A**). Not surprisingly, the evaporation rate was constant throughout the concentration process. Statistical analyses are summarized in **Table S4.**

Figure S10: Dynamic evaporation rates plotted as a function of the volume that has already evaporated in large volume (50 mL) samples. (A) Deionized water and [^{18}F]FHBG mobile phase. (B) NH_4OAc in water solutions. (C) EtOH/water solutions. (D) MeCN/water solutions.

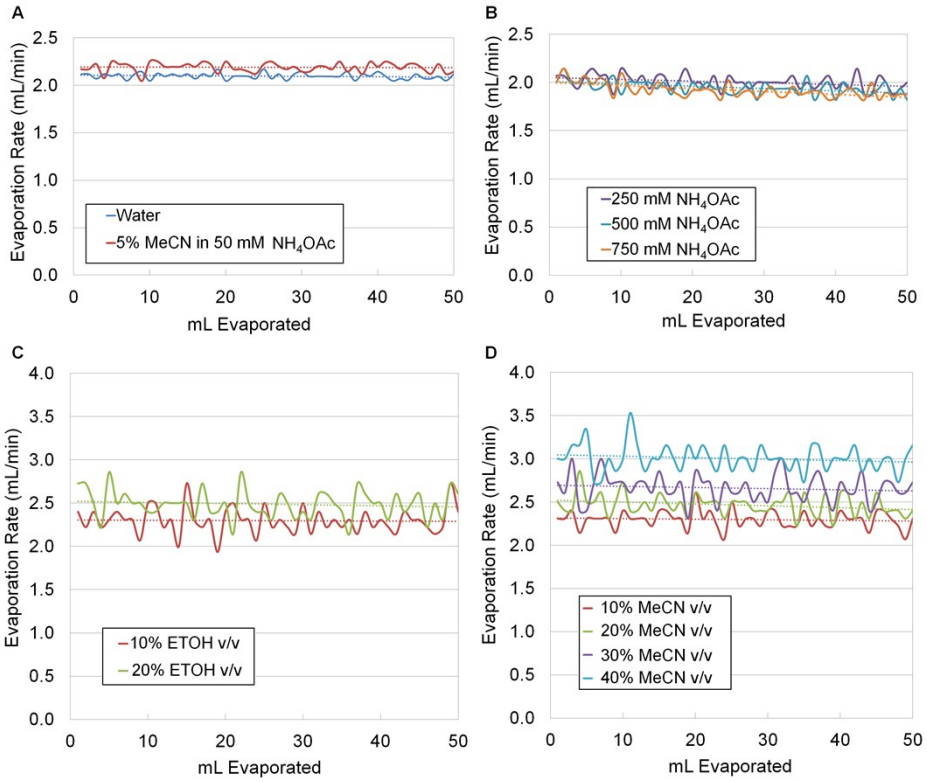

Table S4: Unpaired t-test of evaporation rates at the start (first 5 mL) and at the end (last 5 mL) when evaporating large volume (50 mL) samples.

Sample	Average evaporation rate for first 5 mL	Average evaporation rate for last 5 mL	P-Value	Significant?
Deionized water	2.13 ± 0.06	2.07 ± 0.08	0.13	No
[^{18}F]FHBG mobile phase	2.18 ± 0.07	2.16 ± 0.04	0.29	No
50mM NH_4OAc	2.07 ± 0.08	2.03 ± 0.06	0.19	No
100mM NH_4OAc	2.06 ± 0.08	2.00 ± 0.00	0.06	No
250mM NH_4OAc	2.03 ± 0.06	1.98 ± 0.07	0.13	No
500mM NH_4OAc	2.04 ± 0.06	1.90 ± 0.08	0.01	Yes
750mM NH_4OAc	2.05 ± 0.06	1.86 ± 0.03	0.00	Yes
10% EtOH v/v	2.31 ± 0.09	2.32 ± 0.23	0.45	No
20% EtOH v/v	2.61 ± 0.25	2.47 ± 0.21	0.19	No
10% MeCN v/v	2.29 ± 0.09	2.26 ± 0.12	0.48	No
20% MeCN v/v	2.53 ± 0.19	2.38 ± 0.04	0.38	No
30% MeCN v/v	2.63 ± 0.25	2.68 ± 0.06	0.49	No
40% MeCN v/v	3.13 ± 0.14	2.98 ± 0.16	0.42	No

11 Surface roughness characterization

To better understand the surface roughness differences between sample layers produced with laser ablation vs. traditional milling, sample layers with identical patterns were fabricated using the two techniques. Surface topography was measured using a Dektak 150 Surface Profiler (Veeco Inc, Plainview, NY, USA). The stylus radius used was 12.5 μm, force was set to 3 mg, and the measurement profile was set to measuring hills and valleys. Scanning was performed across the width of the channel. The scan length was set to 6 mm and resulted in a resolution of 0.17 μm per scanned sample.

For each sample, an average height value was obtained for a region of the scan that represents the bottom of the channel. The standard deviation in height was then calculated to quantify the roughness of the channel bottom. For the PMMA layer made by laser ablation, the roughness was 9 μm. For the PEEK sample layer fabricated with traditional milling, the surface was much smoother, with a roughness of 0.6 μm.

12 Total operating time

Total operating time for concentration / formulation for the partial evaporation and complete evaporation methods is given by the following equations:

$$T_{partial} = T_{load} + R_{evap} \times \left(V_{sample} - V_{chip}\right) + T_{delay(partial)} + T_{collect} + N_{rinse} \times T_{rinse}$$

$$T_{complete} = T_{load} + R_{evap} \times \left(V_{sample} - V_{chip}\right) + T_{delay(complete)} + T_{collect} + T_{load} + T_{delay(partial)} + N_{rinse} \times T_{rinse}$$

where:

- T_{load} is the sample loading time (25 s)
- R_{evap} is the evaporation rate
- V_{sample} is the initial sample volume
- V_{chip} is the volume of the chip (~2.75 mL)
- $T_{delay(partial)}$ is the delay time used for partial solvent evaporation (50 s)
- $T_{delay(complete)}$ is the delay time used for complete solvent evaporation (270 s)
- $T_{collect}$ is the time to collect the sample (23 s)
- N_{rinse} is the number of rinse steps
- $T_{rinse} = T_{load} + T_{delay(partial)} + T_{collect}$ is the time required per rinse step

In the case of concentrating a 10 mL sample at a temperature of 100°C with an evaporation rate of 2.0 mL/min, and 2 rinse steps, $T_{partial}$ ~ 8.5 min and $T_{complete}$ ~ 13.5 min. The difference between the two methods arises mainly from the difference in delay time for complete vs partial evaporation (220 s longer for complete evaporation), plus the extra step of loading and concentrating saline prior to collection (25 s + 50 s).

13 In vivo mouse imaging of [^{18}F]D-FAC

[^{18}F]D-FAC was concentrated via conventional rotary evaporation and using the microfluidic concentrator. Rotary evaporation was performed at 80°C with pressure of ~ -10 psi (adjusted to prevent sample bumping during evaporation) before re-suspension in saline. Concentration of [^{18}F]D-FAC in the microfluidic concentrator was carried out at 100°C using the partial evaporation method. A longer than usual final delay time of 110 s was used in the initial concentration and rinse steps to reduce collected sample volume. Two additional rinse plugs were performed with 0.9% sterile saline resulting in a total collected volume of ~1.2mL.

Static scans of the two animals per condition were performed with a microPET scanner (Inveon, Siemens, Washington, D.C., USA). Mice were injected with the formulated tracers (~100 µCi) via the tail vein. After 60 min uptake time, mice were anesthetized with 2% isoflurane and placed in a dedicated imaging chamber with heating. PET images were acquired for 600 s, followed by microCT imaging. PET data was processed by 3D histogramming and reconstruction with a zoom factor of 2.1 using 3D-OSEM with 2 iterations followed by MAP with 18 iterations (beta=0.1). Images were analyzed using AMIDE version 1.0.52. (**Figure S11A, B**) Uptake at 60 min in the bone and bone marrow, thymus, gastrointestinal tract, spleen, and bladder was compared via ROI analysis of the mean injected dose per gram (ID/g). (**Figure S11C**) All animal studies presented in this manuscript were approved by the UCLA IACUC's Animal Research Committee and were carried out following guidelines set by the Department of Laboratory Medicine at UCLA.

Figure S11: PET/CT maximum intensity projection (MIP) image of mouse one hour after injection with [^{18}F]D-FAC concentrated and formulated with (A) a conventional rotary evaporator, and (B) the microfluidic chip in complete evaporation mode. (C) Comparison of biodistribution showing similar uptake in key organs. Values represent average uptake from n=2 animals.

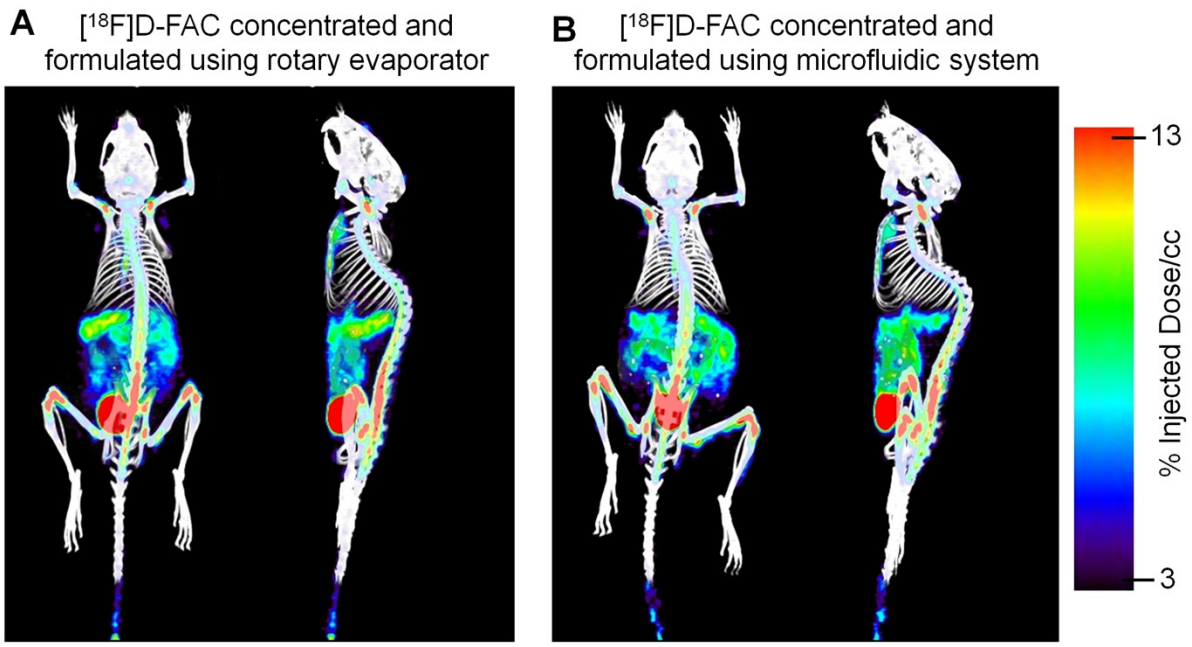

C

Organ	Organ uptake (%ID/cc ± stdev)	
	Rotary evaporator	Microfluidic evaporator
Thymus	6.4 ± 0.3	6.8 ± 0.5
Bone and bone marrow	13.0 ± 0.5	11.0 ± 2.6
Spleen	7.8 ± 0.9	7.1 ± 0.6
Gastrointestinal tract	7.3 ± 0.9	7.0 ± 0.4
Bladder	18.2 ± 1.8	21.1 ± 5.6

14 References

[1] R. Kugel, “Raoult’s Law: Binary Liquid–Vapor Phase Diagrams A Simple Physical Chemistry Experiment,” *J. Chem. Educ.*, vol. 75, no. 9, pp. 1125–1129, 1998.

[2] Wolfram Alpha LLC, “WolframAlpha Computational Knowledge Engine,” *Wolfram|Alpha*. [Online]. Available: www.wolframalpha.com. [Accessed: 15-Jan-2016].

[3] “The ‘Golden Rule’ for Solvent Removal.” Sigma-Aldrich Co, 2007.

[4] R. Hoegger, “Training Papers : Distillation with a Rotary Evaporator.” BÜCHI Labortechnik AG, 1998.